

## Research Article

# Numerical Simulation Research on the Pressure Relief and Permeability Enhancement Mechanism of Large-Diameter Borehole in Coal Seam

Jun Nian , Bo Zhao , and Wei Zhang 

College of Safety and Emergency Management Engineering, Taiyuan University of Technology, Taiyuan 030024, China

Correspondence should be addressed to Bo Zhao; zhaobo91@cqu.edu.cn

Received 4 January 2022; Revised 14 March 2022; Accepted 4 April 2022; Published 26 April 2022

Academic Editor: Peng Hou

Copyright © 2022 Jun Nian et al. This is an open access article distributed under the Creative Commons Attribution License, which permits unrestricted use, distribution, and reproduction in any medium, provided the original work is properly cited.

In order to achieve high-efficiency extraction of coal seams with large-diameter borehole and large flow rates, and to rapidly reduce coal seam gas content and pressure, a large-diameter borehole coal seam pressure relief and permeability enhancement technology is proposed. In this paper, numerical simulation is used to study the mechanism of pressure relief and permeability enhancement in coal seams with large-diameter boreholes, and the evolution of stress, cracks, gas, and permeability of coal bodies around boreholes with different diameters is discussed. The research results show that the stress changes in the coal body around the borehole are symmetrically distributed around the borehole. The stress evolution controls the evolution of the coal body's cracks. Firstly, damage occurs around the borehole and then extends to the upper left and right corners, like a butterfly spreading its wings. The crushing zone increases with the increase of the hole diameter, and the impact radius of the 100-mm, 200-mm, 300-mm, and 350-mm diameter borehole rupture is 0.375 m, 0.65 m, 1.0 m, and 1.25 m, respectively. The rupture radius of the double 350-mm diameter borehole can reach 2.4 m. The larger the diameter of the borehole, the more fissures will be produced, and the air permeability of the coal body in the affected coal seam area will obviously increase. The research results provide theoretical support for gas drainage in soft, low-permeability, high-gas coal seams.

## 1. Introduction

Coal seam permeability restricts the efficiency of gas drainage. Most of the world's coal and gas outburst mines generally have coal seam permeability between  $10^{-4}$  and  $10^{-3}$  mD [1–3]. With the gradual increase in the depth of coal mining, the in situ stress gradually increased, and the permeability of the coal began to gradually decrease [4–8]. This is also the reason for the difficulty of gas drainage. Especially in the structural coal seam, it has the characteristics of poor permeability, high gas content in the coal body, and low strength, which makes it very difficult to extract gas in the coal seam [9–12].

The current conventional antireflection technologies for solving high-gas and low-permeability coal seams include mining pressure relief, hydraulic fracturing, hydraulic slitting, drilling and cavitation, explosive blasting, and carbon dioxide blasting. Mining pressure relief and permeability

enhancement technology changes the gas flow rate in the coal body and the permeability coefficient of the coal body itself, and the gas emission increases, which leads to gas analysis and diffusion in the pores, providing a basis for gas drainage [13–20]. The high-energy liquid disturbance-induced fracturing and antireflection technology uses special liquids to influence the coal body, readjust the stress field, increase the length and number of pores and cracks in the coal body, expand the opening degree, and increase the interconnection area between the coal seams [21–25]. The air permeability coefficient can be brought to the pressure relief requirement [26]. It mainly includes two categories: high-pressure hydraulic fracturing and high-pressure water jet [27–33]. The mechanism of the drilling technology and method is to form a cavity at a specific location in the coal and rock mass, thereby changing the stress of the coal mass, redistributing the pores and gaps in the coal mass, and forming new gaps suitable for the desired state, thereby venting

the coal mass [34–36]. To ensure the safe and efficient mining of high gas and low gas permeability coal seams, the key issue is how to continuously and quickly desorb and release a large amount of adsorbed gas in low gas permeability coal [37–39]. At present, the soft and low-permeability coal seams have the characteristics of small drainage volume, low drainage concentration, and rapid flow attenuation during predrainage, which seriously affects the predrainage effect [40–42].

Studying the mechanism of drilling in soft and low-permeability coal seams to intensify gas drainage; realizing large-aperture, large-flow, and high-efficiency extraction of coal seams; and quickly reducing coal seam gas content and pressure are important issues that need to be resolved urgently. Large-diameter boreholes are used by drilling disturbances. The evolution mechanism of the fissure field, permeability, and seepage field of the coal around the borehole is the prerequisite for revealing the gas migration mechanism and formulating gas drainage technology. Numerical simulation and theoretical analysis of gas migration mechanism in coal seams under different drilling combinations provide theoretical support for gas drainage in soft, low-permeability, high-gas coal seams.

## 2. Principles of Pressure Relief and Permeability Enhancement of Large-Diameter Boreholes in Coal Seams

The gas content equation can be expressed as follows according to the gas content coefficient method:

$$x = A\sqrt{p}, \quad (1)$$

where  $x$  is the gas content in coal and rock mass,  $\text{m}^3/\text{m}^3$ ;  $A$  is the coefficient of coal seam gas content;  $p$  is the gas pressure of coal seam, MPa.

The main difference between the gas-solid coupling equation and the liquid-solid coupling equation is that the compressibility of the gas and the mass change of the adsorption and analysis of the gas are considered.

When the element's stress state or strain state will meet a given damage threshold, the element begins to be damaged, and the elastic modulus of the damaged element is

$$E = (1 - D)E_0, \quad (2)$$

where  $D$  is the damage variable;  $E$  and  $E_0$  are the elastic modulus of damaged and undamaged elements; these parameters are assumed to be scalar.

For uniaxial compression, the breaking criterion of the unit adopts the Mohr Coulomb criterion, namely

$$F = \sigma_1 - \sigma_3 \frac{1 + \sin \varphi}{1 - \sin \varphi} \geq f_c, \quad (3)$$

where  $F$  is the uniaxial force of the unit,  $\sigma_1$  and  $\sigma_3$  are the maximum and minimum principal stresses of the unit,

respectively,  $\varphi$  is the internal friction angle, and  $f_c$  is the uniaxial compressive strength.

When the shear stress reaches the Mohr-Coulomb damage threshold, the damage variable  $D$  is expressed as follows:

$$D = \begin{cases} 0 & \varepsilon < \varepsilon_{c0}, \\ 1 - \frac{f_{cr}}{E_0 \varepsilon} & \varepsilon \leq \varepsilon_{c0}. \end{cases} \quad (4)$$

where  $f_{cr}$  is the uniaxial compressive residual strength;  $\varepsilon_{c0}$  is the maximum compressive strain;  $\varepsilon_r$  is the residual strain. The experiment shows that the damage will cause the air permeability coefficient of time to increase by a few sentences, and the change of the unit air permeability coefficient can be described by the following formula:

$$\lambda = \begin{cases} \lambda_0 e^{-\beta(\sigma_1 - \alpha p)} & D = 0, \\ \xi \lambda_0 e^{-\beta(\sigma_1 - \alpha p)} & D > 0. \end{cases} \quad (5)$$

where  $\lambda_0$  is the initial permeability coefficient;  $P$  is the void pressure;  $\xi$ ,  $\alpha$ ,  $\beta$  is the air permeability coefficient that has increased the magnification, pore pressure coefficient, and coupling coefficient.

## 3. Numerical Analysis of Pressure Relief and Permeability Enhancement of Coal Body Surrounding a Single Hole

The research is carried out on the 3# coal seam of Shiquan Coal Mine. The entire model is composed of coal seams and roof and floor rocks. The borehole diameters are 100 mm, 200 mm, 300 mm, and 350 mm, respectively, to simulate the fracturing and permeability enhancement of the coal around the borehole.

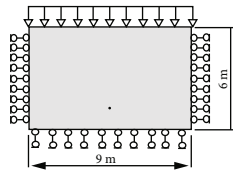
A single-layer coal body is used to establish a model. The length of the coal seam model along the strike is 9 m, the height is 6 m, and the strengthened boreholes are set at a height of 1.2 m. According to the average total thickness of the stratum 178.50 m, the vertical ground pressure is set to 4.0 MPa, and the model is divided into  $360 \times 240$ , a total of 86,400 units.

The boundary conditions are as follows: the two ends are horizontally restrained, the upper end is movable, the bottom end is fixed and restrained, and the air is separated on all sides. The calculation parameters are shown in Table 1.

**3.1. The Law of Pressure Relief and Permeability Enhancement around 100-mm Diameter Borehole.** The simulated maximum principal stress evolution cloud diagram of the coal body around the 100-mm borehole is demonstrated in Figures 1 and 2. It can be seen that during the drilling process, the principal stress is redistributed around the borehole, which has a significant impact on the stability of the coal seam around the borehole. After drilling, the principal stress around the borehole increases sharply, and the distribution is more obvious on both sides of the borehole. The increase in stress around the borehole causes the coal body around the borehole

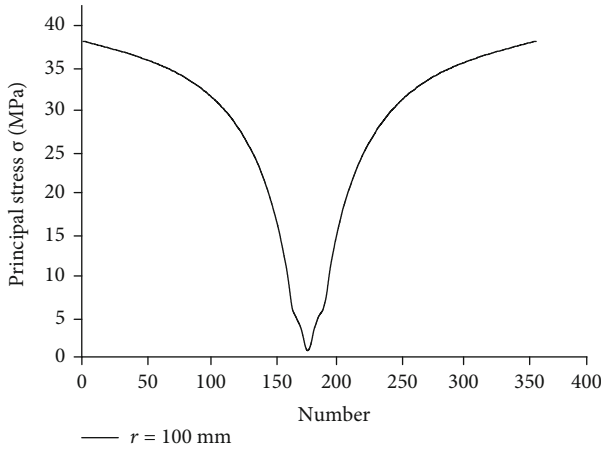
TABLE 1: Model parameters.

Coal seam Parameter	Numerical value
Homogeneity (m)	10
Elastic modulus $E_0$ (GPa)	15
Poisson's ratio $\nu$	0.3
Compressive strength $f_c$ (MPa)	30
Tensile strength $f_t$ (MPa)	4
Coal seam permeability $k$ ( $m^2 \cdot MPa^{-2} \cdot d^{-1}$ )	0.28
Gas pressure $\sigma$ (MPa)	0.56
Coupling coefficient	0.1



Hole  $\Phi$  100 mm

FIGURE 1: 100-mm maximum principal stress for boreholes.



—  $r = 100$  mm

FIGURE 2: Distribution of principal stress.

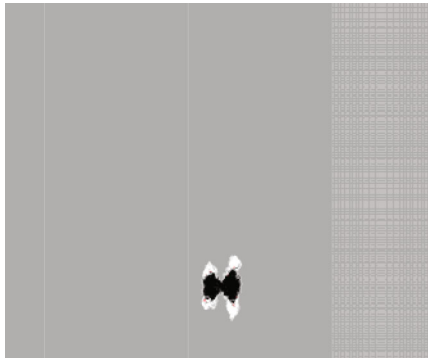
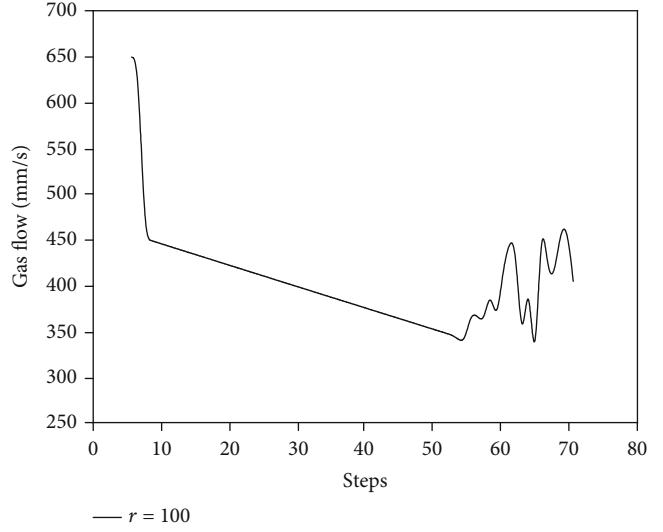
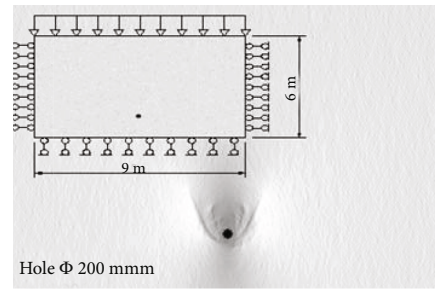


FIGURE 3: 100-mm borehole acoustic emission damage cloud map.



—  $r = 100$

FIGURE 4: Coordinates (175,190) unit gas flow change curve.



Hole  $\Phi$  200 mm

FIGURE 5: 200-mm maximum principal stress for boreholes.

to break, and the stress releases and decreases, forming a pressure relief zone; adjacent coal body stress suddenly increases, followed by destruction, so it continues to extend around the borehole.

After an elliptical fracture zone is formed around the borehole, the main stress increases toward the upper left, upper right, lower left, and lower right of the borehole. The range of the fracture zone further increases, and the final damage zone takes a butterfly shape. Figure 2 shows the stress distribution curve after the coal body is broken (the height is 1.4 m). It can be seen that the coal body stress around the borehole is symmetrically distributed on both sides of the borehole with the borehole as the center.

The process of coal body damage and fracture can be characterized by acoustic emission. Figure 3 is a cloud diagram of the evolution of the acoustic emission process of a 100-mm diameter borehole. It can be seen that when the coal body begins to be damaged, the damage first appears in the horizontal position; then the acoustic emission phenomenon on both sides of the borehole gradually increases, which means that damage continues to form around the borehole, and the damage area is elliptical; the upper left, upper right, lower left, and lower right of the borehole continue to evolve, and the damage becomes more and more

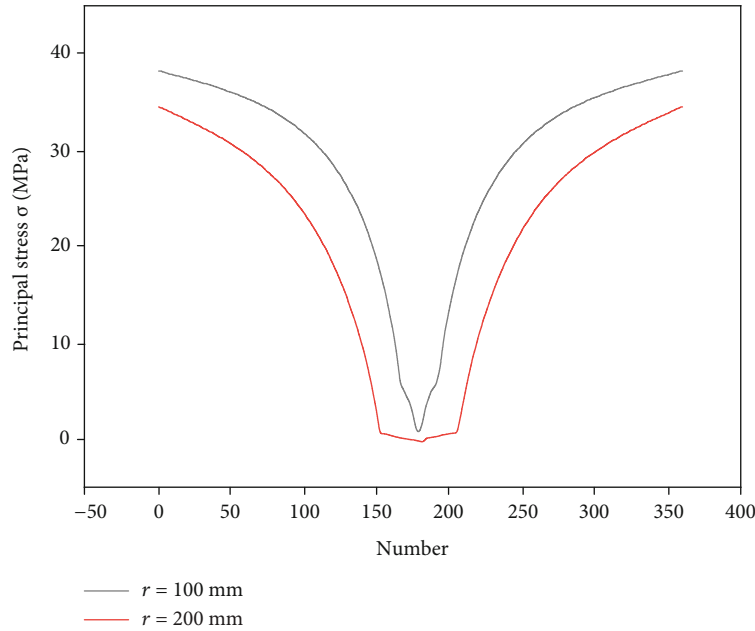


FIGURE 6: 100 mm and 200 mm distribution of principal stress in boreholes.

intense, forming a fissure network around the borehole. The process of coal damage and destruction around the borehole is symmetrically distributed around the borehole. The final damage area around the borehole is butterfly-shaped, and the damage radius of the collapsed hole is about 0.375 m.

After drilling, because the drilling creates cracks and collapses in the surrounding coal body, the stress on the coal body is effectively attenuated, and the air permeability increases, so that the gas originally adsorbed inside the coal body can be released, so that the gas in the borehole can be released. The concentration increased sharply. Figure 4 shows the gas velocity variation diagram of the numerical simulation. It can be seen that the gas emission velocity is very high in the initial stage, and then there is a sudden drop. Gradually slow down, after calculating 50 strides, the gas emission volume has increased volatility. This is because new local damage occurs at the upper left and upper right of the borehole, causing the gas to gush out again in a concentrated manner. Therefore, it is worth pointing out that in the process of coal crushing around the borehole, there may be a phenomenon of gas injection holes due to the accumulation of crushed coal.

*3.2. The Law of Pressure Relief and Permeability Enhancement around 200-mm Diameter Borehole.* Figure 5 explains the evolution cloud diagram of the maximum principal stress caused by the occurrence and expansion of the surrounding coal cracks after a 200-mm diameter hole is drilled. It can be seen that the coal stress around the borehole is symmetrically distributed with the borehole as the center. After the borehole, the surrounding coal stress increases, and the area of change in the horizontal direction is larger. Damage is formed in the stress-concentrated area and continues to expand to the surroundings, and finally the broken area near the borehole

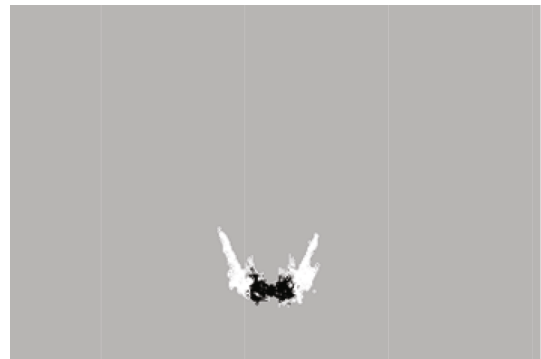


FIGURE 7: 200-mm borehole acoustic emission destruction cloud map.

is elliptical; then the stress on the upper left and upper right of the borehole increases, and at the same time, it extends upward at a certain angle to form the main fracture. From Figure 6, it can be seen that the final damage area as a whole presents a “V” shape with an opening angle of about  $80^\circ$ . The process of weakening the stress around the borehole and forming a broken zone is like the process of “butterfly spreading its wings.”

The 200-mm borehole acoustic emission cloud image is shown in Figure 7. It can be seen that the coal body began to undergo obvious damage in step 49-1. Because the stress on both sides is relatively concentrated, the acoustic emission first appeared in the horizontal position, and the damage continued to proceed around the borehole, forming an elliptical damage area; then damage occurred at the upper left and upper right of the borehole, and the damage occurred at a certain level. The angle continued to extend to the upper part of the coal seam; during the extension

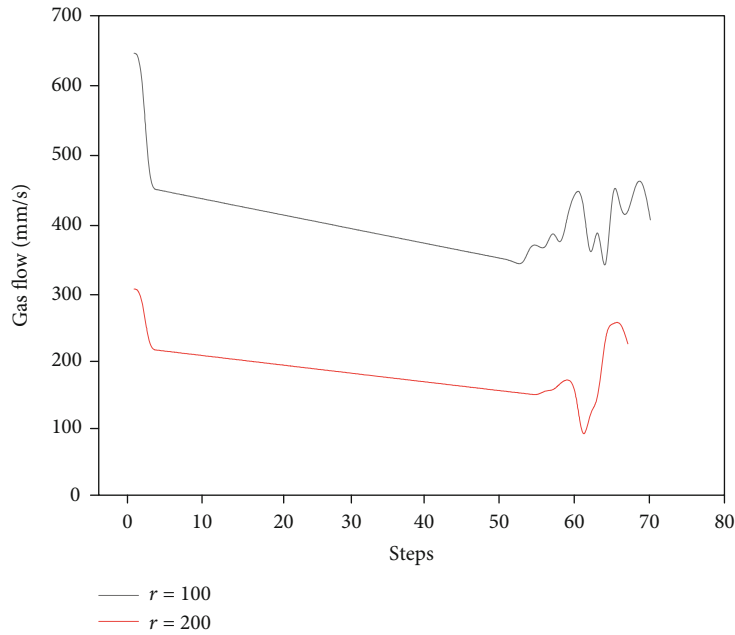


FIGURE 8: 100 mm and 200 mm variation of gas flow in borehole.

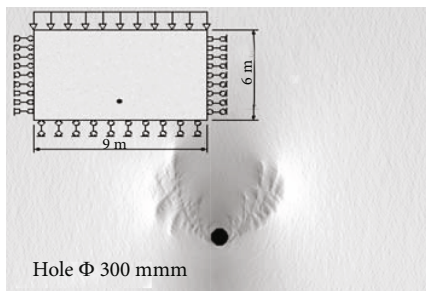


FIGURE 9: 300 mm maximum principal stress for boreholes.

process, the fissures developed more and formed the main fissures, and microfissures continued to appear near the main fissures, and the damage and destruction of the coal body increased; The damage area formed around the hole is “butterfly-shaped” with a damage radius of about 0.65 m.

Compared with the failure evolution process of a 100-mm diameter borehole, the location where the damage begins and the process of damage expansion are roughly the same, and they all show a “butterfly shape” in the end. However, due to the increase in the diameter of the 200 mm borehole, the shear principal stress change area after the borehole is larger, resulting in a wider area of damage to the surrounding coal body, and the process of “butterfly spreading” becomes more obvious.

Figure 8 indicates the comparison curve of the flow change process of 100-mm and 200-mm diameter boreholes. It can be seen that the curves of the gas flow change process of the two are roughly the same, and both have experienced a sharp decrease in gas emission, then the change tends to be flat, and finally the fluctuation increases. Due to the large damage area formed by the 200-mm borehole, the amount

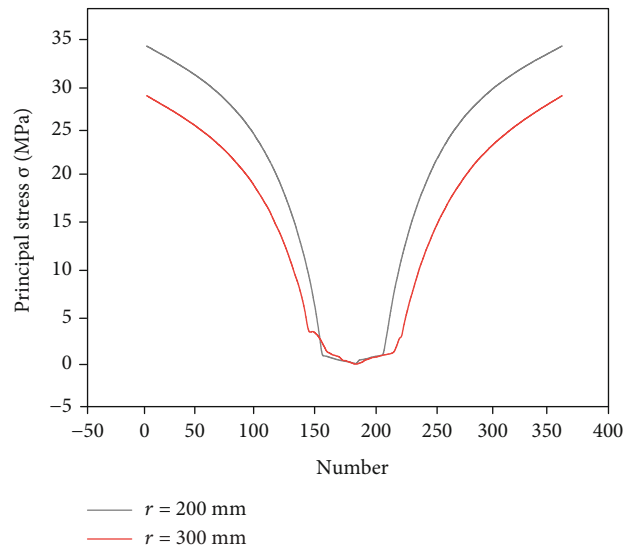


FIGURE 10: Principal stress distribution of 200-mm and 300-mm boreholes.

of newly added gas is large, and the gas attenuation trend is small.

3.3. *The Law of Pressure Relief and Permeability Enhancement around 300-mm Diameter Borehole.* The cloud diagram of the evolution of the maximum principal stress is presented in Figure 9 when the coal cracks around the 300-mm diameter borehole expand. It can be seen that the increase and attenuation of the coal body stress around the borehole is similar to that of 100-mm and 200-mm diameter boreholes; however, the stress attenuation of 300-mm boreholes changes faster, and the number of steps at which



FIGURE 11: 300-mm borehole acoustic emission damage cloud map.

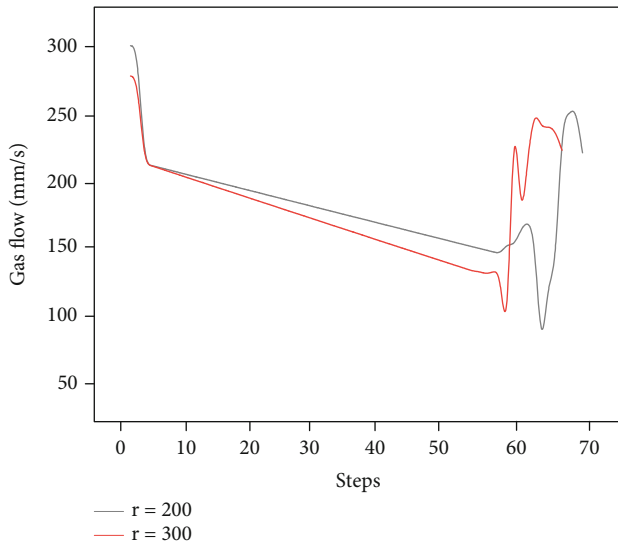


FIGURE 12: Flow changes of 200- and 300-mm holes.

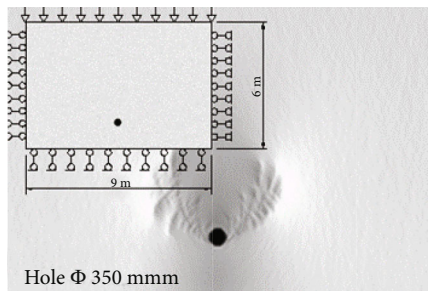


FIGURE 13: Maximum principal stress for 350-mm holes.

failure begins and the number of steps to complete failure are both higher than those of 100 mm. There are fewer holes with a diameter of 200 mm, and the opening angle of the final “V”-shaped crushing zone is larger, with an angle of about  $90^\circ$ .

Figure 10 is the main stress distribution curve of 200-mm and 300-mm diameter boreholes. It can be seen that the main stress distribution trends formed by the failure of the two are roughly the same, and they are distributed symmetrically with the borehole as the center. However, the

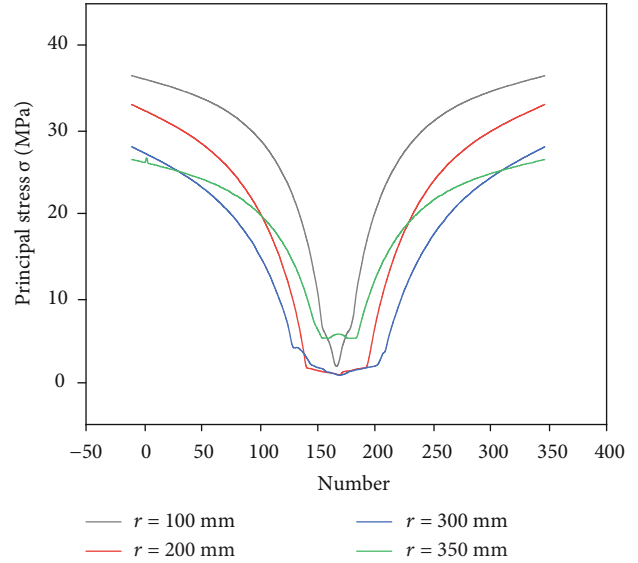


FIGURE 14: Distribution curves of principal stresses for 4 holes.

stress of the 300-mm borehole is lower, because the range of the broken zone formed by the 300-mm borehole is wider, the range of stress attenuation is greater, and the radius of the pressure relief zone formed near the borehole is also larger.

The 300-mm borehole acoustic emission evolution cloud diagram is presented in Figure 11. It can be seen that the coal body acoustic emission evolution around the borehole is symmetrically distributed with the borehole as the center; in the same way, they all show the process of “butterfly spreading their wings.” However, the initial number of acoustic emission steps and the final number of steps after failure of the 300-mm borehole are faster than those of the 100-mm and 200-mm boreholes; the damage area formed around the borehole, the main cracks extending from the upper left and upper right, and the derived fracture network has a wider range, and the damage radius is about 1.0 m.

Figure 12 is a comparison curve of gas flow rate changes for 200-mm and 300-mm diameter boreholes. It can be seen that the gas emission velocity of the two has roughly the same trend; because the area of the 300 mm borehole is larger, the initial emission velocity is lower. In the process of fracture evolution, the number of steps for the gas flow fluctuation phenomenon in the 300-mm diameter borehole due to failure is earlier than that of the 200-mm diameter borehole.

*3.4. The Law of Pressure Relief and Permeability Enhancement around 350-mm Diameter Borehole.* The cloud diagram of the evolution of the maximum principal stress caused by coal cracks around a 350 mm diameter borehole is shown as Figure 13. The stress changes are symmetrically distributed around the borehole. The process of stress increase and attenuation is similar to that of 100-300-mm diameter boreholes, but the 350-mm boreholes produced change faster, the number of steps that start to fail and the number of steps that finally complete failure all are



FIGURE 15: Acoustic emission damage of 350-mm hole cloud map.

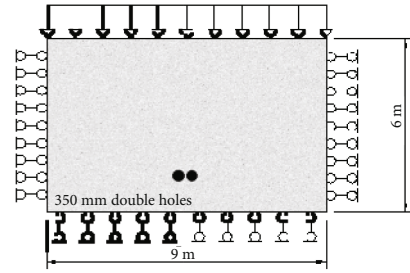


FIGURE 17: Two 350-mm holes model.

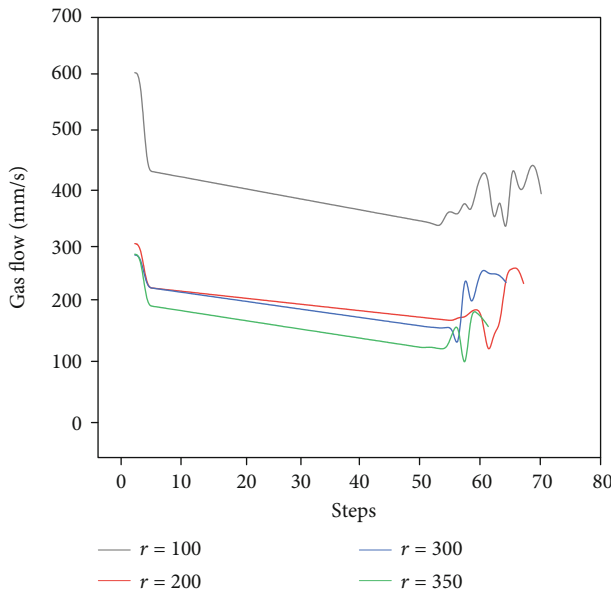


FIGURE 16: Flow patterns of 4 holes.

advanced, and the opening angle of the final “V”-shaped crushing zone is larger, about 110°.

Figure 14 demonstrates the principal stress distribution curves of 4 different diameter boreholes. It can be seen that the coal stresses around the borehole are all symmetrically distributed around the borehole, and the main stress distribution trend is roughly the same. Due to the different radii, the four types of boreholes have different ranges of crushing zones in the surrounding coal body. The larger the borehole, the larger the crushing zone, the larger the stress influence range, the smoother the stress change trend, and the unloading formed near the borehole, the larger the nip area is.

Figure 15 is a cloud diagram of the evolution of the acoustic emission process of a 350-mm diameter borehole. Like the failures caused by the previous drill holes, the acoustic emission evolution is symmetrically distributed with the drill hole as the center. Starting from the calculation step 44-1, damage occurred on both sides of the coal body and continued to form collapsed holes. Then new acoustic emission damage appeared on the upper left and upper right sides of the borehole and continued to move at a certain angle. The upper part of the coal seam stretches to form a macroscopic main fissure. At the same time, microfissures

are derived from the main fissures to form a fissure network, which aggravates the damage and destruction of the coal body, showing a “butterfly-shaped” damage.

Comparing 100-mm, 200-mm, 300-mm, and 350-mm borehole acoustic emission process evolution cloud diagram, it is not difficult to see that coal body damage is symmetrically distributed with the borehole as the center, and the damage start position, damage change, and expansion process are roughly the same, and the damage process performance is “butterfly spreading wings”; however, as the hole diameter of the drill hole becomes larger, the area of coal shear principal stress change around the drill hole is also increasing, and the damage area caused is also increasing. Both the main fissure and the fissure network are enlarged, and the number of steps to form the fissure network is reduced.

Figure 16 explains the change curve of gas flow rate of 4 types of boreholes. It can be seen that the gas emission trends of the 4 types of boreholes are roughly the same. The ruptures formed in the upper left and upper right of the borehole caused the gas flow to suddenly increase and fluctuate.

#### 4. Numerical Analysis of Pressure Relief and Permeability Enhancement around 350-mm Diameter Double Borehole

The model is set to be 9 m long and 6 m high, with a 350-mm double drill hole set at a height of 1.2 m. The model is shown in Figure 17. The number of calculation steps is set to 100 steps, and the calculation is stopped until large cracks are gradually formed around the borehole. The model parameter table is shown in Table 1 above.

The cloud diagram of the maximum principal stress evolution caused by the expansion of coal cracks around 350-mm double boreholes is presented in Figure 18. The stress change process of double boreholes is roughly the same as that of single boreholes: the stress of the surrounding coal body suddenly increases after the borehole is initially drilled, and then the coal body around the borehole is broken to form an elliptical pressure relief zone, as shown in the calculation step 50-1, and then the stress at the upper left and upper right of the borehole starts to increase, extending upwards at a certain angle. When calculating to the last step 57-31, it is obvious that the stress attenuation zone and the

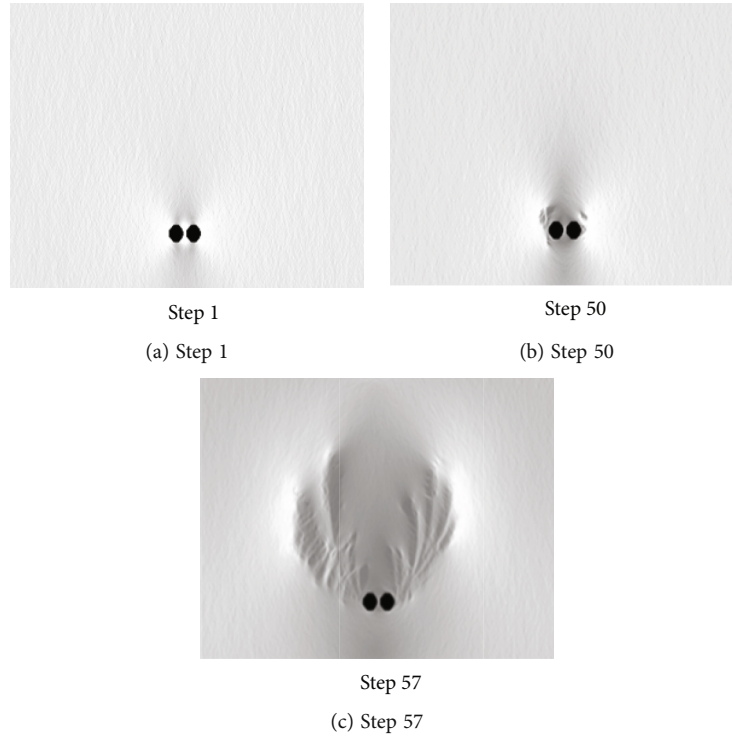


FIGURE 18: Maximum principal stress evolution 350-mm double boreholes.

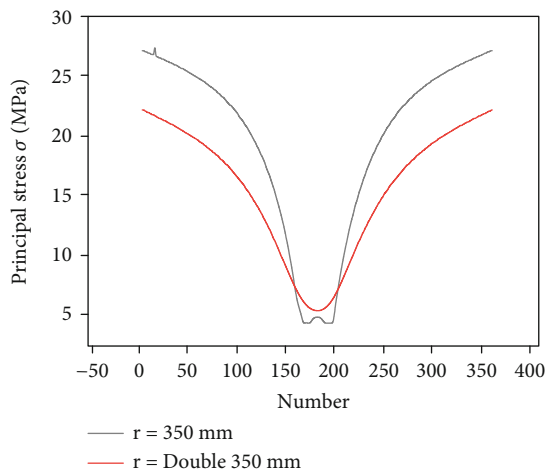


FIGURE 19: Distribution of principal stress in 350-mm single and double holes.

attenuation area formed by the stress change in the upper left and upper right are clearly seen. The overall appearance is a large “V shape” with an angle of approximately  $140^\circ$ . The attenuation process of the stress change of the coal body around the double holes is also like the process of “butterfly spreading its wings.”

Figure 19 is the main stress distribution curve of 350-mm single hole and double hole at 3.5 m height. It can be found that the stress distribution of the two is symmetrically distributed around the center position, and the failure and the final failure time of the 350-mm double hole are earlier



FIGURE 20: Acoustic emission damage cloud of 350-mm double hole.

than the 350-mm single hole, and the stress attenuation change area is larger; in the upper left and upper right of the drill hole, the number of main cracks generated by the square, the distance of expansion, and the range of the formation of the crack network are much larger than that of a single hole, and even the speed of crack expansion is faster than that of a single hole. The final crushing zone of both shows a “V” shape, and the opening angle of the double hole is also larger, about  $140^\circ$ .

Figure 20 is a cloud diagram of the evolution of the acoustic emission process with a 350-mm diameter double hole. The process of borehole acoustic emission damage evolution is symmetrically distributed with the midpoint of the two boreholes as the center. The acoustic emission failure process starts from the 30-1 calculation step, first appears between the two holes, and then appears on both sides of the coal body and continues to evolve. As the destruction progresses, the acoustic emission continues to the upper left and upper right sides of the borehole, forming main fissures. With the main fissures, microfissures are derived to form a fissure network, so that the coal body fissures are fully developed, and the final damage area appears as “butterfly shape”;

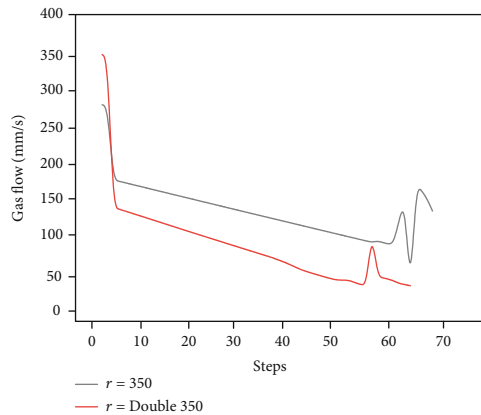


FIGURE 21: Flow chart for 350-mm single and double holes.

as shown in calculation steps 57–31, the damage radius is about 2.4 m.

Comparing the single-hole and double-hole acoustic emission evolution cloud map of 350 mm diameter, the damage and destruction of the coal body around the borehole are distributed symmetrically, and the damage and expansion process are roughly the same, and the damage and expansion form is “butterfly.” The double holes are damaged at the position between the two holes first, the damage area is wider, and the fracture network formed is larger, and then expands on both sides, and the final formation time is shorter.

Figure 21 is a comparison diagram of gas flow between 350-mm single hole and double hole. The gas emission change process of 350-mm single hole and double hole is roughly the same, and both have experienced a process from a sharp drop from the initial position to a gradual change and finally a fluctuation phenomenon with the destruction of the coal body.

## 5. Conclusions

- (1) The stress changes in the coal body around the borehole are symmetrically distributed around the borehole, extending from the vicinity of the borehole to the upper left and upper right at a certain angle, such as a butterfly spreading its wings. The final shape is a “V” shape with an open angle. As it becomes larger and larger, the range of stress influence becomes wider and wider. The failure and the final failure time of the 350-mm double hole are earlier than the 350-mm single hole, and the stress attenuation change area is larger, and the opening angle of the “V”-shaped is also larger
- (2) Stress evolution controls the evolution of coal cracks. First, damage occurs around the borehole and then extends to the upper left and right corners, like a butterfly spreading its wings. The crushing zone increases with the increase of the hole diameter, and the impact radius of the 100-mm, 200-mm, 300-mm, 350-mm diameter borehole rupture is 0.375 m, 0.65 m, 1.0 m, and 1.25 m, respectively. The damage and expansion process of 350-mm double hole is roughly the same as that of 350-mm single hole, but the damage occurs first between the two holes, the final formation time is shorter, and the rupture radius can reach 2.4 m
- (3) Under different diameters, the law of gas emission from coal bodies is roughly the same. As the drilling radius increases, the initial gas emission rate gradually decreases. The larger the diameter of the borehole, the more fissures will be produced, and the air permeability of the coal body in the affected coal seam area will obviously increase. The gas emission change process of 350-mm single hole and double hole is roughly the same

## Data Availability

All data, models, and code generated or used during the study appear in the submitted article.

## Conflicts of Interest

The authors declare that they have no conflicts of interest.

## References

- [1] Y. Cheng and Z. Pan, “Reservoir properties of Chinese tectonic coal: a review,” *Fuel*, vol. 260, p. 116350, 2020.
- [2] N. Kursunoglu and M. Onder, “Application of structural equation modeling to evaluate coal and gas outbursts,” *Tunnelling and Underground Space Technology*, vol. 88, pp. 63–72, 2019.
- [3] B. Zhao, J. Cao, H. Sun, G. Wen, D. Linchao, and B. Wang, “Experimental investigations of stress-gas pressure evolution rules of coal and gas outburst: a case study in Dingji coal mine, China,” *Energy Science & Engineering*, vol. 8, pp. 61–73, 2020.
- [4] B. Zhao, G. Wen, J. Nian et al., “Numerical simulation study on the multi-physical field response to underground coal and gas outburst under high geo-stress conditions,” *Minerals*, vol. 12, no. 2, p. 151, 2022.
- [5] F. Yan, J. Xu, S. Peng et al., “Effect of capacitance on physico-chemical evolution characteristics of bituminous coal treated by high-voltage electric pulses,” *Powder Technology*, vol. 367, pp. 47–55, 2020.
- [6] L. Jiang, Q. Wu, Q. Wu et al., “Fracture failure analysis of hard and thick key layer and its dynamic response characteristics,” *Engineering Failure Analysis*, vol. 98, pp. 118–130, 2019.
- [7] S. Lu, Y. Zhang, Z. Sa, and S. Si, “Evaluation of the effect of adsorbed gas and free gas on mechanical properties of coal,” *Environment and Earth Science*, vol. 78, no. 6, 2019.
- [8] P. Hou, S. Su, X. Liang et al., “Effect of liquid nitrogen freeze-thaw cycle on fracture toughness and energy release rate of saturated sandstone,” *Engineering Fracture Mechanics*, vol. 258, p. 108066, 2021.
- [9] Q. Zou, H. Liu, Y. Zhang, Q. Li, J. Fu, and Q. Hu, “Rationality evaluation of production deployment of outburst-prone coal mines: a case study of nantong coal mine in Chongqing, China,” *Safety Science*, vol. 122, p. 104515, 2020.
- [10] Z. Wei, Y. Cheng, P. Guo, K. Jin, and H. Wang, “An analysis of the gas-solid plug flow formation: new insights into the coal

- failure process during coal and gas outbursts,” *Powder Technology*, vol. 305, pp. 39–47, 2017.
- [11] B. Zhou, J. Xu, F. Yan, S. Peng, and L. Cheng, “Effects of gas pressure on dynamic response of two-phase flow for coal-gas outburst,” *Powder Technology*, vol. 377, pp. 55–69, 2021.
- [12] F. An, Y. Yuan, X. Chen, Z. Li, and L. Li, “Expansion energy of coal gas for the initiation of coal and gas outbursts,” *Fuel*, vol. 235, pp. 551–557, 2019.
- [13] W. Yang, H. Wang, B. Lin et al., “Outburst mechanism of tunnelling through coal seams and the safety strategy by using “strong-weak” coupling circle-layers,” *Tunnelling and Underground Space Technology*, vol. 74, pp. 107–118, 2018.
- [14] Q. Shi, B. Qin, H. Liang, Y. Gao, Q. Bi, and B. Qu, “Effects of igneous intrusions on the structure and spontaneous combustion propensity of coal: a case study of bituminous coal in Daxing Mine, China,” *Fuel*, vol. 216, pp. 181–189, 2018.
- [15] T. Zhao, W. Guo, Y. Tan, Y. Yin, L. Cai, and J. Pan, “Case studies of rock bursts under complicated geological conditions during multi-seam mining at a depth of 800 m,” *Rock Mechanics and Rock Engineering*, vol. 51, no. 5, pp. 1539–1564, 2018.
- [16] C. Fan, D. Elsworth, S. Li, L. Zhou, Z. Yang, and Y. Song, “Thermo-hydro-mechanical-chemical couplings controlling CH<sub>4</sub> production and CO<sub>2</sub> sequestration in enhanced coalbed methane recovery,” *Energy*, vol. 173, pp. 1054–1077, 2019.
- [17] A. Fisne and O. Esen, “Coal and gas outburst hazard in Zonguldak Coal Basin of Turkey, and association with geological parameters,” *Natural Hazards*, vol. 74, no. 3, pp. 1363–1390, 2014.
- [18] N. Skoczylas, B. Dutka, and J. Sobczyk, “Mechanical and gaseous properties of coal briquettes in terms of outburst risk,” *Fuel*, vol. 134, pp. 45–52, 2014.
- [19] L. Wang, Y. Cheng, F. An, H. Zhou, S. Kong, and W. Wang, “Characteristics of gas disaster in the Huaibei coalfield and its control and development technologies,” *Natural Hazards*, vol. 71, no. 1, pp. 85–107, 2014.
- [20] S. Xue, L. Yuan, Y. Wang, and J. Xie, “Numerical analyses of the major parameters affecting the initiation of outbursts of coal and gas,” *Rock Mechanics and Rock Engineering*, vol. 47, no. 4, pp. 1505–1510, 2014.
- [21] R. Zhang, Z. Jiang, H. Zhou, C. Yang, and S. Xiao, “Groundwater outbursts from faults above a confined aquifer in the coal mining,” *Natural Hazards*, vol. 71, no. 3, pp. 1861–1872, 2014.
- [22] H. Zhou, Q. Yang, Y. Cheng, C. Ge, and J. Chen, “Methane drainage and utilization in coal mines with strong coal and gas outburst dangers: a case study in Luling mine, China,” *Journal of Natural Gas Science and Engineering*, vol. 20, pp. 357–365, 2014.
- [23] S. Wang, D. Elsworth, and J. Liu, “Permeability evolution during progressive deformation of intact coal and implications for instability in underground coal seams,” *International Journal of Rock Mechanics and Mining*, vol. 58, pp. 34–45, 2013.
- [24] F. An, Y. Cheng, L. Wang, and W. Li, “A numerical model for outburst including the effect of adsorbed gas on coal deformation and mechanical properties,” *Computers and Geotechnics*, vol. 54, pp. 222–231, 2013.
- [25] Y. Lu, J. Tang, Z. Ge, B. Xia, and Y. Liu, “Hard rock drilling technique with abrasive water jet assistance,” *International Journal of Rock Mechanics and Mining*, vol. 60, pp. 47–56, 2013.
- [26] M. B. Díaz Aguado and C. González Nicieza, “Control and prevention of gas outbursts in coal mines, Riosa–Olloniego coalfield, Spain,” *International Journal of Coal Geology*, vol. 69, no. 4, pp. 253–266, 2007.
- [27] M. B. Wold, L. D. Connell, and S. K. Choi, “The role of spatial variability in coal seam parameters on gas outburst behaviour during coal mining,” *International Journal of Coal Geology*, vol. 75, no. 1, pp. 1–14, 2008.
- [28] C. Jiang, C. Wang, X. Li, Y. Chen, Q. Xie, Y. Liu et al., “Quick determination of gas pressure before uncovering coal in cross-cuts and shafts,” *Journal of China University of Mining and Technology*, vol. 18, no. 4, pp. 494–499, 2008.
- [29] F. Chaojun, L. Sheng, D. Elsworth, H. Jun, and Y. Zhenhua, “Experimental investigation on dynamic strength and energy dissipation characteristics of gas outburst-prone coal,” *Energy Science & Engineering*, vol. 8, no. 4, pp. 1015–1028, 2020.
- [30] F. Chaojun, L. Sheng, D. Luo Mingkun, and Y. Z. Wenzhang, “Coal and gas outburst dynamic system,” *International Journal of Mining Science and Technology*, vol. 27, no. 1, pp. 49–55, 2017.
- [31] J. Sobczyk, “The influence of sorption processes on gas stresses leading to the coal and gas outburst in the laboratory conditions,” *Fuel*, vol. 90, no. 3, pp. 1018–1023, 2011.
- [32] Z. Xusheng, H. Qianting, and N. Xiaoliang, “Research on comprehensive early-warning technology of coal and gas outburst,” *Procedia Engineering*, vol. 26, pp. 2376–2382, 2011.
- [33] B. Huang, C. Liu, J. Fu, and H. Guan, “Hydraulic fracturing after water pressure control blasting for increased fracturing,” *International Journal of Rock Mechanics and Mining*, vol. 48, no. 6, pp. 976–983, 2011.
- [34] C. Ö. Karacan, F. A. Ruiz, M. Cotè, and S. Phipps, “Coal mine methane: a review of capture and utilization practices with benefits to mining safety and to greenhouse gas reduction,” *International Journal of Coal Geology*, vol. 86, no. 2–3, pp. 121–156, 2011.
- [35] T. Lu, Z. Zhao, and H. Hu, “Improving the gate road development rate and reducing outburst occurrences using the water-jet technique in high gas content outburst-prone soft coal seam,” *International Journal of Rock Mechanics and Mining*, vol. 48, no. 8, pp. 1271–1282, 2011.
- [36] Q. Hu, S. Zhang, G. Wen, L. Dai, and B. Wang, “Coal-like material for coal and gas outburst simulation tests,” *International Journal of Rock Mechanics and Mining*, vol. 74, pp. 151–156, 2015.
- [37] X. Chen, G. Ma, C. Fan, and S. Ge, “Research progress of coal damage under unsteady load in China,” *Geofluids*, vol. 2021, Article ID 5610391, 13 pages, 2021.
- [38] P. Hou, Y. Xue, F. Gao et al., “Effect of liquid nitrogen cooling on mechanical characteristics and fracture morphology of layer coal under Brazilian splitting test,” *International Journal of Rock Mechanics and Mining Sciences*, vol. 151, p. 105026, 2022.
- [39] F. Yan, B. Lin, J. Xu et al., “Structural evolution characteristics of middle-high rank coal samples subjected to high-voltage electrical pulse,” *Energy & Fuels*, vol. 32, no. 3, pp. 3263–3271, 2018.
- [40] F. Chaojun, W. Haiou, L. Sheng, B. Gang, and Z. Lijun, “Coal seam gas extraction by integrated drillings and punchings from the floor roadway considering hydraulic-mechanical coupling effect,” *Geofluids*, vol. 2022, Article ID 5198227, 10 pages, 2022.

- [41] F. Chaojun, Y. Lei, W. Gang, H. Qiming, F. Xiang, and W. Haiou, "Investigation on coal skeleton deformation in CO<sub>2</sub> injection enhanced CH<sub>4</sub> drainage from underground coal seam," *Frontiers in Earth Science*, vol. 9, p. 766011, 2021.
- [42] Z. Bo, W. Guangcai, Q. Ma, S. Haitao, Y. Fazhi, and N. Jun, "Distribution characteristics of pulverized coal and stress–gas pressure–temperature response laws in coal and gas outburst under deep mining conditions," *Energy Science & Engineering*, pp. 1–19, 2022.